Dynamic modeling platform for series hybrid electric vehicles

Simos A Evangelou * **Wassif Shabbir** *

* *Department of Electrical and Electronic Engineering, Imperial College London, UK (e-mail: s.evangelou@imperial.ac.uk, wassif.shabbir07@imperial.ac.uk).*

Abstract: This paper introduces a simulation model that can be used to develop and test designs and control systems for hybrid electric vehicles (HEVs). The work involves a novel simulating platform, developed in Simulink, where each component of a series HEV is developed using a first-principles approach in a modular fashion, validated by available experimental data and then integrated to form a coupled nonlinear dynamic model. The vehicle model is capable to act as a platform for the design of supervisory control systems (SCSs) that optimize the energy flow in the powertrain. Simulations with two distinct SCSs and two driving cycles are used to analyze the vehicle performance under varying driving and operating conditions. The results demonstrate the applicability of the model for realistic prediction of both vehicle behavior and component energy losses, design optimization and control system design.

Keywords: Modelling, hybrid electric vehicle, supervisory control, energy management

1. INTRODUCTION

Due to environmental concerns, alternatives to the conventional vehicle are sought and the Hybrid Electric Vehicle (HEV) has emerged as a viable part of the solution. To facilitate this transition and to ensure a cost effective and rapid development of new HEV designs, it is greatly beneficial to employ modeling and simulation tools to explore and optimize designs. By now, there have been numerous studies on the subject of modeling and simulation of HEVs, however the academic literature has mainly focused on the modeling of particular HEV components, rather than the integration of entire vehicle models Van Mierlo et al. (2004); Liu and Peng (2008); Doucette and McCulloch (2011). The latter modeling capability is provided by various commercial modeling software tools, such as ADVISOR, AVL CRUISE, PSAT, PSIM and others, that are readily available.

Notwithstanding the activity in this area, it is believed that currently available modeling platforms do not yet include sufficient modeling detail or flexibility, nor are they sufficiently validated, to satisfy the objectives for which they are built. These include: (a) to help identify which aspects of the design, from component to system level, need to be modified for optimal overall operation, for example in terms of fuel economy, emissions and acceleration, (b) to study the transient behavior of each component and how it interacts with the integrated vehicle system, and (c) to improve performance by designing clever control schemes both for individual components and for the supervision of the integrated powertrain to enable optimal energy flow management. Existing models often rely on static look-up tables and performance maps that omit important transient characteristics, or on simple power-request dynamics that do not allow for the accurate scaling or for the adjustment of critical design parameters.

The present work aims to create a high-fidelity modeling and control tool that is capable of both fast computation and accurate dynamic simulation of HEVs. The task involves the modeling and control of the individual subsystems of the vehicle and its powertrain, and their integration into a coherent system model, presently of series powertrain architecture. The aim is to develop experimentally validated flexible component models in the form of equations derived from first principles, in an object-oriented manner, so that they can be used broadly in the construction of system models of any powertrain topologies beyond the series one. A key issue is therefore the accurate description of the interdependencies between the subsystems. A further important aspect of the present task is to develop SCSs that manage the energy flow in the overall system to propel the vehicle, and to achieve enhanced system efficiency and other objectives.

The paper is organized as follows. In Section 2 the component models of the HEV and their integration to an overall system model are described. Key characteristics of the models are descriptions for the hybrid-electric drive powertrain, regenerative braking, vehicle dynamics, and component-level controls. Section 3 describes the system level supervisory controllers used to regulate the energy flow through the vehicle components. Simulations of two driving cycles are conducted and the results are presented and discussed in Section 4. Finally, conclusions are drawn in Section 5.

2. COMPONENT MATHEMATICAL MODELING

The hybrid vehicle considered in this work utilizes a series powertrain topology and represents a class of passenger vehicles that are appropriate for urban and extra-urban transportation. Its general structure, including the powertrain, is shown in Figure 1.

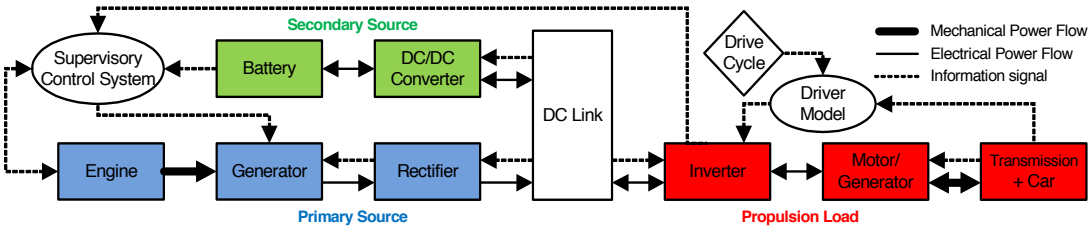


Fig. 1. Overall structure of series hybrid vehicle powertrain and main body. Thin and thick arrows correspond to electrical and mechanical energy flow respectively, while the direction of the arrows shows the direction of the flow.

The powertrain comprises: a common DC-link of 700 V, on which there are connected the Primary Source (PS) – a diesel internal combustion engine (ICE) and a Permanent Magnet Synchronous Generator (PMSG) with the associated AC/DC converter (rectifier); the Secondary Source (SS) – a battery with the associated DC/DC converter; and, the Propulsion Load (PL) – a Permanent Magnet Synchronous Motor (PMSM) with the associated DC/AC converter (inverter), together with the car. The car includes the body masses, transmission, suspension, tires and aerodynamics. The supervisory controller decides the power flow between the various powertrain components, and acts in response to the commands of a driver model that is used to enable the following of speed demands corresponding to specific driving cycles. The component models are first constructed in causal form in Simulink, with appropriate choice of inputs and outputs, and are subsequently interconnected via their inputs and outputs, and control feedback loops, to obtain the overall model. The modeling work presented here is an evolution of the work presented in Evangelou and Shukla (2012).

2.1 Propulsion Load

Car Accurate car response requires accurate representation of the longitudinal car behavior. The model built describes the longitudinal car dynamics and it is based on the multibody model presented in Thommyppillai et al. (2009), capable of general motions. The main ingredients of the model are a main body with forward and vertical translation, and pitch rotation, suspension, spinning wheels, rear wheel connection to the motor shaft via continuously variable transmission (CVT), aerodynamic lift and drag forces proportional to the square of the speed, vertically compliant and slipping tyres, tyre rolling resistance proportional to tire normal load, and regenerative braking. The parameter values used in the model are representative of a contemporary European family saloon and are taken from Thommyppillai et al. (2009), where the total mass is 1475.6 kg, the pitch inertia is 2152.1 kgm^2, and the drag coefficient is 0.35.

Permanent Magnet Synchronous Motor (PMSM) In the present work a surface mounted PMSM has been used. The associated 3-phase circuit diagram of the star-connected PMSM can be seen on the right part of Figure 2. ω_{sm} is the inverter frequency in (electrical) rad/s. The inverter frequency and the rotor speed, ω_{rm}, are related according to $\omega_{sm} = p_m \omega_{rm}$ in which p_m is the number of pole pairs per phase in the stator. The 3-phase dynamic equations can be expressed in terms of the standard 2-phase rotor

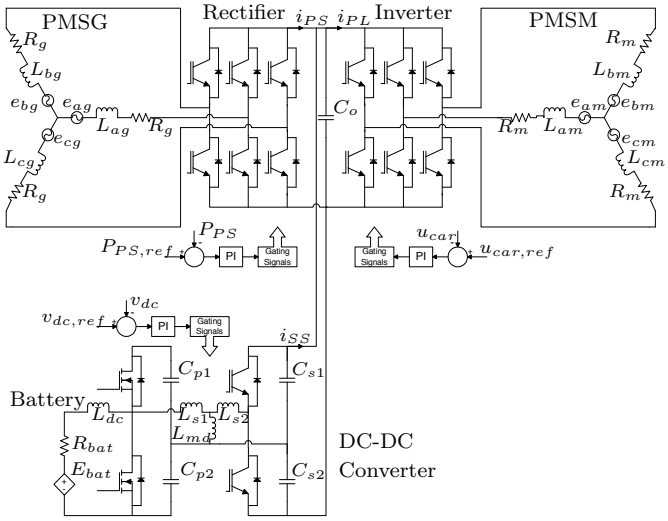


Fig. 2. Circuit diagram showing the electrical connection of the generator (PMSG), AC/DC rectifier, battery, DC/DC converter, DC/AC inverter and motor (PMSM). Symbols R, L and e represent phase resistances, inductances and induced emfs respectively. Subscripts a, b and c correspond to the individual phases, and subscripts g, m and ref correspond to 'generator', 'motor' and 'reference'. E_{bat} and R_{bat} correspond to the battery emf and internal resistance, while L_{dc}, L_{s1}, L_{s2}, L_{md}, C_{p1}, C_{p2}, C_{s1} and C_{s2} are inductances and capacitances associated with the DC/DC converter. i_{PS}, i_{SS} and i_{PL} denote the primary source (generator-branch), secondary source (battery-branch) and propulsion load (motor-branch) dc currents. C_0 is the DC-link capacitor, v_{dc} is the DC-link voltage, P_{PS} is the primary source power and u_{car} is the forward speed of the car. The signals related to the control of v_{dc}, P_{PS} and u_{car} are also shown.

d-q rotating reference frame Pillay and Krishnan (1989) as follows:

$$\frac{di_{dm}}{dt} = (v_{dm} - R_m i_{dm} + \omega_{sm} L_{qm} i_{qm})/L_{dm}, \quad (1)$$

$$\frac{di_{qm}}{dt} = (v_{qm} - R_m i_{qm} - \omega_{sm}(L_{dm} i_{dm} + \lambda_{fm}))/L_{qm}, \quad (2)$$

where i_{dm} and i_{qm} are the d- (direct) and q- (quadrature) axis components of stator current, v_{dm} and v_{qm} are the d- and q-axis components of stator voltage, L_{dm} and L_{qm} are the d- and q-axis stator inductances, and R_m is the stator resistance. The electromagnetic torque produced by the motor is given by Pillay and Krishnan (1989)

Table 1. Parameters for PMSM and PMSG.

Parameter	Symbol	PMSM	PMSG
Nominal rated power	P_n	75 kW	92 kVA
Maximum speed	ω_n	5000 rpm	5000 rpm
Stator resistance	R	0.04 Ω	0.08 Ω
D-axis stator inductance	L_d	0.20 mH	0.45 mH
Q-axis stator inductance	L_q	0.20 mH	0.45 mH
Rotor magnetic flux	λ_f	0.125 Wb	0.220 Wb
Moment of inertia	J	0.05 kgm^2	0.05 kgm^2
Number of pole pairs	p	6	6

$$T_{em} = \frac{3}{2} p_m \left(\lambda_{fm} i_{qm} + (L_{dm} - L_{qm}) i_{dm} i_{qm}\right). \quad (3)$$

In the case that $L_{dm} = L_{qm}$ (surface-mounted PMSM), or when i_{dm} is forced to zero, the electromagnetic torque in Equation (3) becomes

$$T_{em} = \frac{3}{2} p_m \lambda_{fm} i_{qm}. \quad (4)$$

This torque is reduced by a friction torque, T_{fm}, to produce a load toque, T_{lm}, according to $T_{lm} = T_{em} - T_{fm}$. T_{lm} is applied on the rotor shaft that is connected to the car transmission, thereby driving the car forward. T_{fm} is included in the model to represent mechanisms of energy dissipation in the PMSM beyond the losses due to copper windings resistance. An identification of the friction torque and PMSM constant parameters is performed to give a qualitatively correct prediction of the steady-state motor efficiency in comparison with experimentally measured efficiency profiles EVO-Electric (2010b), and is found to be rotor-speed dependent as illustrated in Figure 3. As it can be seen, at low speeds it involves some familiar characteristics of mechanical friction, such as static and coulomb friction type behaviors. The unknown PMSM

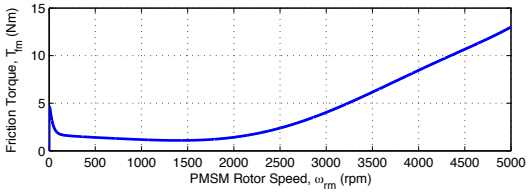


Fig. 3. Variation of the PMSM frictional torque, T_{fm}, with rotor speed, ω_{rm}.

parameters are identified by also taking into account other aspects of the PMSM, such as the voltage operating envelopes. The overall parameters are shown in Table 1.

In the present application we control the forward speed of the car by controlling the speed of the motor which is driving the car. This is achieved by utilizing the vector control approach by controlling separately the quadrature current, i_{qm}, that is producing the torque, and the direct current, i_{dm}, that is producing the flux which is parallel to the rotor flux Pillay and Krishnan (1989). Under the assumptions made in Equation (4), the electromagnetic torque is linearized and is directly proportional to the q-axis current. A typical control scenario is one in which the torque per ampere is maximized by maximizing i_{qm}. This is achieved by forcing i_{dm} to zero since at any time the inequality $\sqrt{{i_{dm}}^2 + {i_{qm}}^2} \leq I_{max}$ has to be satisfied, where I_{max} is the maximum current the motor can withstand Krishnan (2010). In the present application, two inner current PI control loops are used to set the v_{dm} and v_{qm} values respectively so that i_{dm} becomes zero ($i_{dm,ref} = 0$) and i_{qm} provides the required torque. The i_{qm} reference is obtained from an outer PI loop that operates on the error between the speed reference signal, possibly arising from a defined drive profile, and the actual speed of the car, calculated in the car dynamics model described in Section 2.1.1. The block diagram of the overall motor control scheme can be seen on the right part of Figure 4. The PI gains in each case have been found by trial and error.

Three-phase DC to AC converter (Inverter) A bidirectional pulse width modulated (PWM) inverter Mohan et al. (2002) is considered to drive the PMSM, as shown in Figure 2. It can be shown that the overall average model of the PWM inverter in the d-q frame is given by the following equations Burgos et al. (2006); Schauder and Mehta (1993):

$$i'_{PL} = \frac{3}{2}(d_{qm} i_{qm} + d_{dm} i_{dm}), \quad (5)$$

$$v_{dm} = d_{dm} v_{dc}, \quad (6)$$

$$v_{qm} = d_{qm} v_{dc}, \quad (7)$$

in which v_{dc} is the DC-link voltage, i'_{PL} is the modified DC current drawn by the inverter from the DC-link, and d_{dm}, d_{qm} are continuous duty cycle functions in the d and q axis respectively. Since the inverter model is assumed to apply smooth voltages to the motor windings, the instantaneous values of d_{dm} and d_{qm} can be obtained from Equations (6) and (7) and the actual values of v_{dc}, v_{dm} and v_{qm}. Hence the ideal inverter model requires inputs from v_{dm}, v_{qm}, v_{dc}, i_{dm} and i_{qm} and calculates i'_{PL} according to Equation (5). It is also necessary to restrict the maximum value of the phase voltages since the inverter cannot produce at any time an output voltage which is higher than a certain fraction of its DC input voltage; with space vector modulation this fraction is $1/\sqrt{3}$ Wallmark (2004); Krause et al. (2013). In our model we use saturation functions to constrain v_{dm} and v_{qm} as follows

$$\sqrt{{v_{dm}}^2 + {v_{qm}}^2} \leq \frac{v_{dc}}{\sqrt{3}}, \quad (8)$$

which is also related to the inverter remaining in its linear range of operation (modulation index ≤ 1).

The power losses in the converter are accounted for by scaling the total current drawn by the inverter as follows:

$$i_{PL} = \begin{cases} \frac{1}{\eta_{inv}} i'_{PL} & i'_{PL} \geq 0 \\ \eta_{inv} i'_{PL} & i'_{PL} < 0 \end{cases} \quad (9)$$

in which η_{inv} is the inverter average efficiency. In the present work $\eta_{inv} = 95\%$ Shen et al. (2007); Rotering and Ilic (2011).

CVT A CVT is considered in the present work. The overall average power efficiency of this transmission is taken into account by scaling the load torque on the transmission shaft, as follows:

$$T'_{lm} = \eta_{CVT} T_{lm} \quad T_{lm} \geq 0, \quad T'_{lm} = \frac{1}{\eta_{CVT}} T_{lm} \quad T_{lm} < 0$$

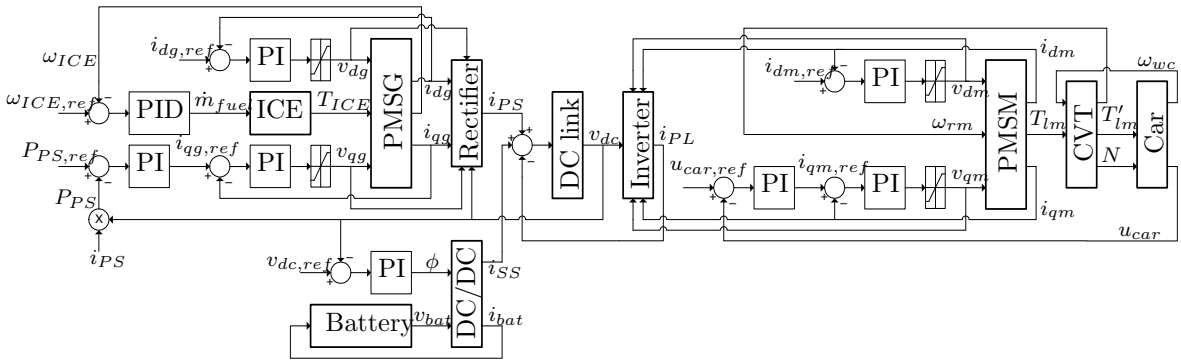


Fig. 4. Interconnection of the ICE, PMSG, rectifier, battery, DC/DC converter, inverter, PMSM, transmission (CVT) and car, and the related control loops. Symbols v_d, i_d, v_q and i_q represent d-q voltages and currents respectively, while subscripts g, m and ref correspond to 'generator', 'motor' and 'reference'. ω_{ICE} is the rotational speed of the ICE, $\dot{m}_{fuel}$ is the ICE fuel mass rate demand, T_{ICE} is the ICE torque, ω_{rm} is the speed of the PMSM rotor, T_{lm} is the PMSM load torque, N is the transmission gear ratio, ω_{wc} is the wheel rotational speed, ϕ is the phase shift variable of the DC/DC converter, v_{bat} and i_{bat} are the battery voltage and current respectively.

where η_{CVT} is the average efficiency of the CVT, which typically ranges from 89% to 94% Miller (2003). In our work the value of average efficiency of the toroidal CVT, $\eta_{CVT} = 93\%$, is used Heath (2007); Delkhosh et al. (2011). The final drive ratio of the CVT is controlled to be $N_{ref} = |T'_{lm}|/(k_{CVT}\,\omega_{wc})$, to achieve operation of the motor in its most efficient operating region, according to the scheme described in Shabbir and Evangelou (2014a). k_{CVT} is a constant and ω_{wc} is the wheel rotational speed.

2.2 Primary Source

Engine (ICE) The engine model employed has been built as part of our research program and it includes low frequency engine transient dynamics Shukla (2012): a) emptying and filling models for the inlet and outlet manifolds, b) mean-value torque maps for the engine cylinders, the turbocharger turbine and turbocharger compressor, c) engine and turbocharger inertias, and d) fuel-injection valve dynamics. The ICE parameter set is based on a turbocharged Puma 2.0L diesel engine. The fuel mass flow rate serves as an input and the ICE torque, acting on the common engine-generator shaft (see Section 2.2.2), is designated as an output.

Permanent Magnet Synchronous Generator (PMSG) The PMSG is a PMSM operated in the 'fourth quadrant', in which the rotor speed is still positive but the current has reverse flow and the torque generated in the machine has the opposite sign (negative) as compared to 'first-quadrant' operation for the motoring case Krishnan (2010). Therefore, with a change of notation (subscripts 'm' in the symbols changed to 'g') the PMSM equations presented in Section 2.1.2 are used to model the PMSG, with the corresponding values of the relevant variables simply allowed to change sign.

The generator rotor is linked to the ICE inertia via a fixed gear ratio G, such that $\omega_{rg} = G\omega_{ICE}$, where ω_{rg} is the generator rotor speed and ω_{ICE} is the ICE speed. Therefore the mechanical dynamics of the generator are governed by the following equation:

$$GT_{ICE} + G^2(T_{eg} - T_{fg}) = (J_{ICE} + G^2 J_g)\frac{d\omega_{rg}}{dt}, \quad (10)$$

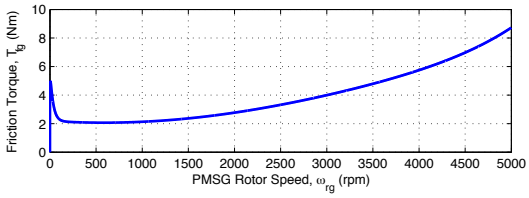


Fig. 5. Variation of the PMSG frictional torque, T_{fg}, with PMSG rotor speed, ω_{rg}.

with T_{ICE} the mechanical torque applied by the ICE on its inertia, T_{eg} the electromagnetic torque applied by the PMSG on its shaft, T_{fg} the friction torque in the generator, and J_{ICE} ($0.22\,\text{kgm}^2$ in this work) and J_g the moments of inertia of the ICE and generator respectively.

Using a similar analysis to the one conducted for the PMSM in Section 2.1.2, a PMSG friction torque and constant parameters $(T_{fg}, R_g, \lambda_{fg}, p_g)$ are chosen so that the predicted power out, P_{outg}, represents well the trends in experimental data EVO-Electric (2010a) as PMSG efficiency, η_g, and ω_{rg} vary. The overall parameters are shown in Table 1. The variation of the proposed friction torque with rotational speed is shown in Figure 5.

Due to the series topology of the powertrain, the ICE is only used to drive the PMSG and its speed is independent of the wheel speed. G is chosen to be 1 in the present work to choose respective speeds at which both the ICE and the PMSG operate most efficiently. The angular velocity of the PMSG rotor (and consequently of the ICE) is controlled via a PI feedback loop that sets the fuel mass rate input to the ICE to produce the required torque on the common engine-generator inertia, to overcome the opposing electromagnetic and friction torques; see Equation (10). While the PMSG is driven at the desired angular speed the amount of electrical power it is delivering to the DC-link can be regulated by the AC to DC converter. The PMSG power control scheme involves a fast inner current control loop and a slower outer power control loop, similarly to the vector control approach of the PMSM in Section 2.1.2. The upper left part of Figure 4 illustrates the control strategy in diagrammatic form.

Three-phase AC to DC converter (Rectifier) The PMSG is interfaced to the DC-link via a PWM rectifier Mohan et al. (2002), as shown in Figure 2. Average modeling of the switching dynamics is again considered, with the average model of a rectifier being the same as the one for the inverter in Section 2.1.3. Equations similar to (5)-(7) are used to determine the modified DC 'input' current of the rectifier, i'^{*}_{PS} (the illustrated rectifier current is defined as $i_{PS} = -i^{*}_{PS}$ to correspond to a non-negative-valued PS output power P_{PS}, which is more meaningful for the ICE component). The maximum voltages that can be formed at the generator terminals by the PWM rectifier are physically limited by the actual value of the DC-link voltage. Therefore v_{dg} and v_{qg} are restricted with appropriate saturation functions as in the case of the motor; see Equation (8). The power losses in the rectifier are accounted for by the same scaling of the total current as in the case of the inverter in Section 2.1.3, and amount to a constant rectifier efficiency of η_{rec} (in the present work $\eta_{rec} = \eta_{inv} = 95\%$) Shen et al. (2007); Rotering and Ilic (2011). The total DC current 'drawn' by the rectifier is thus shown to be $i^{*}_{PS} = \eta_{rec} i'^{*}_{PS}$. This is applicable only for $i^{*}_{PS} \leq 0$ since this rectifier current can only flow in one direction, opposite to the one corresponding to current being drawn by an inverter.

2.3 Secondary Source

Battery A Li-ion battery model based on the work presented in Shepherd (1965); Tremblay and Dessaint (2009) is used. It is able to capture the generic dynamic response of a Li-ion battery, and it can establish a relationship among its state of charge (SOC), open circuit voltage and current demand as follows:

$$Q = (1 - SOC_{init}) \cdot Q_{max} + \int_0^t i_{bat} dt \tag{11}$$

$$i^{*}_{bat} = \frac{1}{\tau_r s + 1} i_{bat} \tag{12}$$

$$E_{bat} = \begin{cases} E_0 - \dfrac{Q_{max} \cdot K_1 Q}{Q_{max} - Q} - \dfrac{Q_{max} \cdot K_2 i^{*}_{bat}}{Q_{max} - Q} \\ \qquad + A \exp(-B \cdot Q) & i^{*}_{bat} \geq 0 \\ E_0 - \dfrac{Q_{max} \cdot K_1 Q}{0.1 Q_{max} + Q} - \dfrac{Q_{max} \cdot K_2 i^{*}_{bat}}{Q_{max} - Q} \\ \qquad + A \exp(-B \cdot Q) & i^{*}_{bat} < 0 \end{cases} \tag{13}$$

$$v_{bat} = E_{bat} - R_{bat} \cdot i_{bat} \tag{14}$$

$$SOC = 1 - \frac{Q}{Q_{max}} \tag{15}$$

Q represents the consumed charge, i_{bat} the average current drawn from the battery, and E_{bat} the battery voltage before the voltage drop across R_{bat}, the battery internal resistance; see Figure 2. The i^{*}_{bat} variable is a filtered version of i_{bat} flowing through the polarization resistance ('s' in (12) is the standard Laplace variable). Equation (13) shows both the discharging and charging dynamics, which are considered separately due to differences in the polarization resistance. In the battery model i_{bat} is the input and v_{bat} is the output as shown in Figure 4. The model parameters are chosen to represent a stack of Li-ion cells arranged to provide a maximum rated capacity of 20 Ah and maximum rated voltage of 250 V.

DC to DC converter The battery is connected to the DC-link via a bidirectional DC/DC converter, as shown in Figure 2. A converter that utilizes a zero-voltage-switching (ZVS) bidirectional dual half-bridge topology is employed. A switching-frequency-dependent average model for this converter has been derived in Li et al. (2001) to predict its dynamic characteristics in both power flow directions. The average model equations, adjusted to the present application, are as follows:

$$\frac{di_{bat}}{dt} = -\frac{R_{bat}}{L_{dc}} i_{bat} - \frac{1}{2L_{dc}} v_{12} + \frac{1}{L_{dc}} E_{bat}, \tag{16}$$

$$\frac{dv_{12}}{dt} = \frac{1}{C_p} i_{bat} - \frac{2}{C_p} \frac{\phi(\pi - \phi)}{4\pi\omega_c L_s} v_{dc}, \tag{17}$$

$$i'_{SS} = \frac{\phi(\pi - \phi)}{4\pi\omega_c L_s} v_{12}, \tag{18}$$

with v_{12} the combined average voltage across the C_{p1} and C_{p2} capacitors on the lower voltage side, ω_c the switching frequency (in rad/s), ϕ the phase shift between the switching waveforms of the low and high voltage sides, L_{dc} and L_s internal inductances and i'_{SS} the modified average current provided to the DC-link by the converter. With reference to the circuit diagram in Figure 2, it can be pointed out that once we employ the averaged model, L_{md} is removed, and L_{s1} and L_{s2} combine to a single inductance L_s. Also, $C_{p1} = C_{p2} = C_p$. The parameter values for this converter in SI units are $L_{dc} = 5 \times 10^{-5}$, $L_s = 8 \times 10^{-7}$, $C_p = 10^{-2}$ and $\omega_c = 1.257 \times 10^5$. The phase shift ϕ is an input variable that is used to control the DC-link voltage at the desired value, $v_{dc,ref}$. This control scheme, involving one PI loop, is shown in block diagram form in the lower left part of Figure 4. The power loss of the converter is represented by an average efficiency η_{dcdc} and current scaling as for the inverter and rectifier:

$$i_{SS} = \begin{cases} \eta_{dcdc} i'_{SS} & i'_{SS} \geq 0 \\ \dfrac{1}{\eta_{dcdc}} i'_{SS} & i'_{SS} < 0 \end{cases} \tag{19}$$

In the present work $\eta_{dcdc} = 96\%$ Pahlevaninezhad et al. (2012).

2.4 Integration of component models

The overall electrical integration of the three groups of components, PS, SS and PL already described, is done at the DC-link for this series HEV architecture. As it can be seen in Figure 2 the DC-link between the AC/DC, DC/DC and DC/AC converters is a capacitor that gets charged and discharged by the currents flowing in and out the various converters according to

$$i_{PS} + i_{SS} - i_{PL} = C \frac{dv_{dc}}{dt}, \tag{20}$$

in which $C = C_0 + C_s/2$ where $C_s/2$ corresponds to the series arrangement of the C_{s1} and C_{s2} capacitors ($C_s = C_{s1} = C_{s2}$). The values $C_0 = 1$ mF and $C_s = 10$ mF are used. Four paths of energy flow are involved: a) ICE to PMSG to PMSM to car (PS driving), b) Battery to PMSM to car (SS driving), c) Car to PMSM to battery (regenerative braking), and d) ICE to PMSG to battery (charging). Hybrid modes are also possible. All the modes

of operation are enabled by controlling separately the three electronic converters, with each control achieving a different task, as shown in Figure 2 and as explained in Sections 2.1.2, 2.2.2 and 2.3.2. With this separation of roles between the PMSG and battery the demanded load power is served partially by the PMSG, while the remaining power is provided or absorbed by the battery which acts as an energy equalizer with fast dynamics.

3. SUPERVISORY CONTROL

The supervisory control system (SCS) primarily has the task of managing how the powertrain of the vehicle meets load demand. It decides the extent to which the ICE and/or battery power the motor. Two distinct control schemes from the popular literature are implemented to offer a sufficiently wide perspective on the performance of the vehicle model. Further work on SCSs using the developed model has been presented in Shabbir and Evangelou (2014b).

3.1 Thermostat Control System

The series architecture allows the ICE to operate at a speed that is independent of the speed of the vehicle and wheels, enabling it to consistently operate at its optimal point. This insight is the focal point of the Thermostat control system (TCS) Ehsani et al. (2010), where the ICE is operated at its optimal point in torque and engine speed whenever it is used. Typically, the load requirements of the PMSM, P_{PL}, will not be in perfect match with the optimal power produced by the PS, P_{PS}, therefore the battery acts as an equalizer, absorbing or delivering any discrepancy in power. The battery power under these circumstances is given by $P_{SS} = P_{PL} - P_{PS}$. This mode of operation is used until the SOC of the battery reaches its upper threshold, SOC_U, at which point the ICE is requested to idle and the battery alone powers the vehicle. As the battery eventually reaches its lower threshold, SOC_L, the ICE is again activated to operate at its optimal point. For the present model the PS operates at its optimal efficiency at an ICE speed of 1700 rpm and power demand of 22 kW Shabbir and Evangelou (2014b), and SOC_L and SOC_U have been set to 50% and 80% respectively. It has also been decided that the vehicle will begin operating in battery only operation. The SCS of the vehicle is implemented in Simulink using the Stateflow library. The implementation in the form of a state-machine allows robust and intuitive design of control laws.

3.2 Power Follower Control Strategy

Another conventional control scheme for series HEVs is the Power follower control strategy (PFCS) Salmasi (2007). The basic principle is based upon the understanding that the efficiency of the battery decreases as power requirement increases, while the efficiency of the ICE improves. Thus, when the load from the PMSM (P_{PL}) is low and SOC is high, the SS is selected to deliver the power to the vehicle ($S(t) = 0$). Conversely, when P_{PL} is high or SOC is low, the PS is selected to meet the load ($S(t) = 1$).

For $S(t) = 0$, we always have $P_{PS} = 0$. For $S(t) = 1$, the operation of the PS is defined as

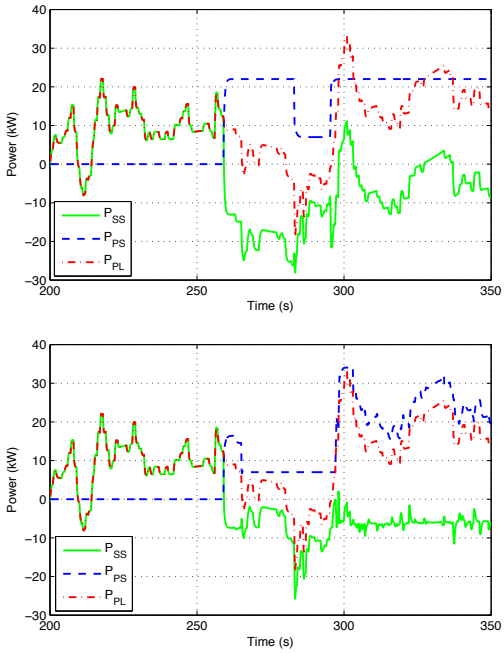


Fig. 6. Load distribution profile for the TCS (top) and PFCS (bottom), for a window of the HWFET cycle.

$$P_{PS}(t) = \begin{cases} P_{PSmin} & SOC(t) \geq SOC_U \\ P_m(t) & SOC_L < SOC(t) < SOC_U \\ P_{PSmax} & SOC(t) \leq SOC_L \end{cases} \quad (21)$$

where P_m is given by

$$P_m(t) = P_{PL} + P_{ch}\left[\frac{SOC_U + SOC_L}{2} - SOC(t)\right]. \quad (22)$$

As shown, the PS is essentially following the load P_{PL} when the SOC is at the midpoint between SOC_L and SOC_U, but biases the operation in favor of charging or discharging the SS in the cases of low and high SOC respectively. The bias is scaled by P_{ch} which is tuned to optimize fuel economy ($P_{ch} = 0.5$ in this work). Note that in general $P_{SS} \neq 0$ when $S(t) = 1$. The PFCS, as the TCS, is implemented using the Stateflow library.

4. SIMULATION RESULTS

The energy flows of the vehicle as a whole are studied by simulations to appreciate the nature of the SCS and the energy losses throughout the vehicle. The results have been generated for two distinct American driving cycles corresponding to two distinct types of driving: a) the NYCC (New York City Cycle), representing urban driving at low-speed with frequent stop-and-go characteristics, and b) the HWFET (Highway Fuel Economy Test) corresponding to highway driving with a sustained high-speed profile.

4.1 Sources power split

Simulations are run to investigate how each of the two control strategies presented in Section 3 (TCS and PFCS) choose to operate to meet the load requirements of the PMSM; see Fig. 6. It is clear that both the SCSs are delivering the same amount of power, although the power distribution between the SS and the PS are very different.

The TCS initially operates only using the SS, with the ICE idling. However, as the SOC drops to 50% the vehicle begins using the PS at its optimal point of operation (22 kW) while the SS acts as an equalizer. When the PS is active, the SS typically ends up being charged by absorbing surplus power (shown as negative power in the chart) but when the power request is higher than 22 kW the SS provides supplementary power. It is worth noting that the PS temporarily reduces it's supply of power around $t = 280$ s during regenerative breaking, to avoid extreme charging of the SS. The PFCS also operates only using the SS to begin with, but as the SOC reaches 50% the SCS switches to hybrid mode, as defined in (21). In this mode, the PS provides the power requested by PL and also some surplus power proportional to the SOC deviation from the initial SOC.

4.2 Sources energy usage

The different natures of the two SCSs result in distinct energy flows through the vehicle, as shown in Fig. 7. It is clear that the TCS uses the ICE significantly less for NYCC and significantly more for HWFET compared to the PFCS. This can be understood from the principle that the TCS operates very often from the ICE at a high load during highway driving, while it lets the battery operate almost exclusively during urban driving. Accordingly, for the NYCC driving cycle, the ICE usage is only marginally higher than the ICE friction losses due to the extensive idling (which is energy spent solely on overcoming friction). However, in the case of the HWFET driving cycle, we observe comparable ICE friction losses for the TCS and the PFCS, even though the ICE is used significantly more for the former. This reflects the fact that the TCS operates at very close to its optimal efficiency point, unlike the PFCS.

Comparing the battery discharging for the two SCSs, it becomes clear that the TCS uses the battery more during urban driving but to a similar extent on the highway. However, the battery charging differs significantly. When TCS is used to drive the NYCC, the SS is used almost exclusively to drive the PL, and thus the battery is essentially only recharged using regenerative braking. The PFCS on the other hand activates the PS when a high power is requested, and thereafter operates the PS to charge the battery, leading to a very high amount of battery charging. Conversely, there is very limited regenerative braking during highway driving so as the SOC drops to its lower limit the TCS uses the PS to charge the battery, as was shown previously in Figure 6. Consequently, at the end of the HWFET driving cycle, the TCS has accumulated a significant amount of reserve charge. While the stored energy in the battery has been taken into account to compute the total energy consumption of the SCS, the higher quality of the stored energy is not considered. Essentially, the energy stored in the battery was originally generated from the ICE and has already suffered the associated losses, which are not considered in the total energy comparison. The comparison could be made more valid by computing an equivalent energy consumption (taking into consideration the higher quality of the battery energy). However, the aim of this paper is to demonstrate the operation of the vehicle when simulated and the effect on energy flow depending on

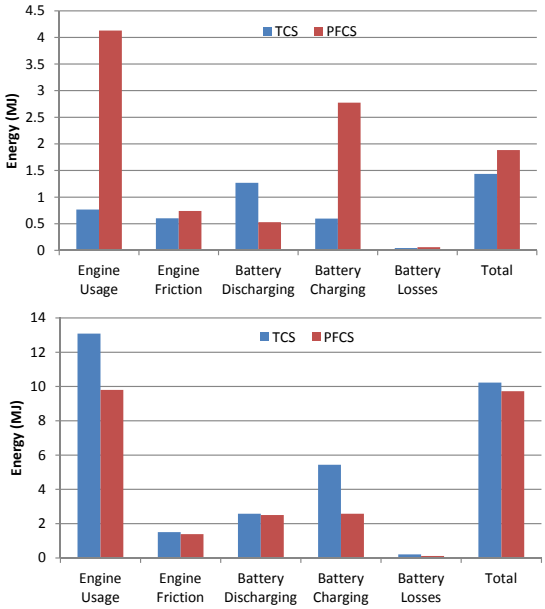


Fig. 7. Comparison of energy flow from ICE and battery for two SCSs for the urban NYCC driving cycle (top) and for the extra-urban HWFET cycle (bottom).

choice of SCS, rather than benchmarking the fuel economy of SCSs. Thus, the presented data is sufficient to illustrate the impact the choice of SCS has on the energy consumption of the vehicle, and by extension to give an indication on the fuel economy.

4.3 Vehicle and powertrain energy losses

Results are also collected for energy losses elsewhere in the vehicle model and are presented in Fig. 8 for NYCC and HWFET. As expected, the energy losses in the inverter, PMSM, transmission, tires and aerodynamic drag are independent of the SCS and are only determined by the speed profile. As is also expected from the discussion of the energy usage in the vehicle, the TCS suffers lower DC/DC converter losses for the NYCC driving cycle as it uses the battery (charging and discharging combined) to a lesser extent than the PFCS. It is also noteworthy that the TCS barely has any PMSG resistance and rectifier losses for NYCC as the PS is very rarely used to power the vehicle. The high PMSG friction losses are almost exclusively attributable to the idling losses. For the HWFET driving cycle, the TCS has higher losses in almost every single category. This follows from the fact that it not only uses the PS more than the PFCS, but it also uses the SS more.

The charts in Fig. 8 also serve the function of illustrating the relative magnitude of the losses throughout the vehicle model. As expected, the aerodynamic losses are prevalent in highway driving, while the tire losses are more important in city driving. Also, the transmission losses (CVT) are larger than the PMSM losses for both driving cycles. Lastly, it is clear that losses associated with power electronics are significant and should not be neglected.

5. CONCLUSIONS

The modeling work that has been presented has the potential to act as a platform for: a) the modeling and

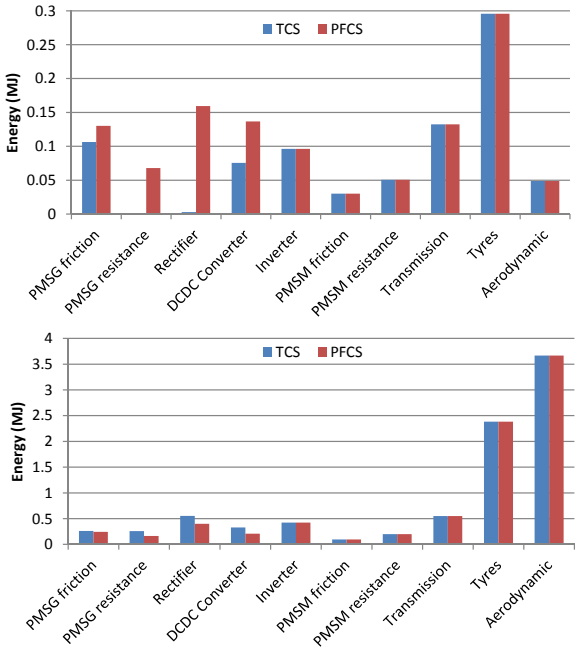


Fig. 8. Comparison of energy losses throughout the vehicle for two SCSs for the urban NYCC driving cycle (top) and for the extra-urban HWFET cycle (bottom).

analysis of HEVs with various powertrain architectures, b) the development of sophisticated supervisory controllers that enhance significantly the fuel savings, and c) the optimal selection and sizing of components, and overall design optimization of the car and its powertrain.

REFERENCES

Burgos, R.P., Kshirsagar, P., Lidozzi, A., Wang, F., and Boroyevich, D. (2006). Mathematical model and control design for sensorless vector control of permanent magnet synchronous machines. In *Computers in Power Electronics, IEEE Workshops on*, 76–82.

Delkhosh, M., Foumani, M.S., Boroushaki, M., Ekhtiari, M., and Dehghani, M. (2011). Geometrical optimization of half toroidal continuously variable transmission using particle swarm optimization. *Scientia Iranica*, 18(5).

Doucette, R.T. and McCulloch, M.D. (2011). A comparison of high-speed flywheels, batteries, and ultracapacitors on the bases of cost and fuel economy as the energy storage system in a fuel cell based hybrid electric vehicle. *Journal of Power Sources*, 196(3), 1163 – 1170.

Ehsani, M., Gao, Y., and Emadi, A. (2010). *Modern electric, hybrid electric, and fuel cell vehicles: fundamentals, theory, and design*. CRC press.

Evangelou, S.A. and Shukla, A. (2012). Advances in the modelling and control of series hybrid electric vehicles. In *Proceedings of 2012 American Control Conference*. IEEE, Montreal, Canada.

EVO-Electric (2010a). *AFG-140 Axial Flux Generator*.

EVO-Electric (2010b). *AFM-140 Axial Flux Motor*. UK.

Heath, R.P.G. (2007). Seamless AMT offers efficient alternative to CVT. In *JSAE Annual Congress*.

Krause, P.C., Wasynczuk, O., Sudhoff, S.D., and Pekarek, S. (2013). *Analysis of Electric Machinery and Drive Systems*. Wiley-IEEE Press, 3rd edition.

Krishnan, R. (2010). *Permanent magnet synchronous and brushless DC motor drives*. CRC Press, Boca Raton.

Li, H., Peng, F.Z., and Lawler, J.S. (2001). A natural ZVS high-power bi-directional dc-dc converter with minimum number of devices. *Industry Applications Conference, Thirty-Sixth IAS Annual Meeting*, 3, 1874–1881.

Liu, J. and Peng, H. (2008). Modeling and control of a power-split hybrid vehicle. *Control Systems Technology, IEEE Transactions on*, 16(6), 1242–1251.

Miller, J.M. (2003). *Propulsion Systems for Hybrid Vehicles*. The Institution of Engineering and Technology, UK. ISBN-13 978-0863413360.

Mohan, N., Undeland, T.M., and Robbins, W.P. (2002). *Power Electronics: Converters, Applications, and Design*. John Wiley & Sons, USA.

Pahlevaninezhad, M., Das, P., Drobnik, J., Jain, P.K., and Bakhshai, A. (2012). A novel ZVZCS full-bridge DC/DC converter used for electric vehicles. *IEEE Transactions on Power Electronics*, 27(6), 2752–2769.

Pillay, P. and Krishnan, R. (1989). Modelling, simulation, and analysis of permanent-magnet motor drives, Part I: The permanent-magnet synchronous motor drive. *IEEE Transactions on Industry Application*, 25(2), 265–273.

Rotering, N. and Ilic, M. (2011). Optimal charge control of plug-in hybrid electric vehicles in deregulated electricity markets. *IEEE Trans. Power Sys.*, 26(3), 1021–1029.

Salmasi, F. (2007). Control strategies for hybrid electric vehicles: Evolution, classification, comparison, and future trends. *IEEE Transactions on Vehicular Technology*, 56(5), 2393–2404.

Schauder, C. and Mehta, H. (1993). Vector analysis and control of advanced static var compensators. *Proc. Inst. Elect. Eng.*, 140, 299–306.

Shabbir, W. and Evangelou, S.A. (2014a). Efficiency analysis of a continuously variable transmission with linear control for a series hybrid electric vehicle. In *IFAC World Congress*, 6264–6269.

Shabbir, W. and Evangelou, S.A. (2014b). Real-time control strategy to maximize hybrid electric vehicle powertrain efficiency. *Applied Energy*, 135, 512–522.

Shen, M., Joseph, A., Wang, J., Peng, F.Z., and Adams, D.J. (2007). Comparison of traditional inverters and Z-source inverter for fuel cell vehicles. *IEEE Transactions on Power Electronics*, 22(4), 1453–1463.

Shepherd, C.M. (1965). Design of primary and secondary cells - part 2. An equation describing battery discharge. *Journal of Electrochemical Society*, 112, 657–664.

Shukla, A. (2012). *Modelling and Simulation of Hybrid Electric Vehicles*. Ph.D. thesis, Imperial College.

Thommyppillai, M., Evangelou, S.A., and Sharp, R.S. (2009). Advances in the development of a virtual car driver. *Multibody System Dynamics*, 22, 245–267.

Tremblay, O. and Dessaint, L.A. (2009). Experimental validation of a battery dynamic model for EV applications. *World Electric Vehicle J.*, 3, .

Van Mierlo, J., Van den Bossche, P., and Maggetto, G. (2004). Models of energy sources for EV and HEV: fuel cells, batteries, ultracapacitors, flywheels and engine-generators. *Journal of power sources*, 128(1), 76–89.

Wallmark, O. (2004). *On control of permanent-magnet synchronous motors in hybrid-electric vehicle applications*. Ph.D. thesis, Chalmers University of Technology.